

Confronting sparse Gaia DR3 photometry with TESS for a sample of around 60,000 OBAF-type pulsators

Daniel Hey¹  and Conny Aerts^{2,3,4} 

¹ Institute for Astronomy, University of Hawai'i, Honolulu, HI 96822, USA
email: dhey@hawaii.edu

² Institute of Astronomy, KU Leuven, Celestijnenlaan 200D, B-3001 Leuven, Belgium
email: Conny.Aerts@kuleuven.be

³ Department of Astrophysics, IMAPP, Radboud University Nijmegen, PO Box 9010, 6500 GL, Nijmegen, The Netherlands

⁴ Max Planck Institute for Astronomy, Koenigstuhl 17, 69117, Heidelberg, Germany

Received February ??, 2024; Accepted ??, 2024

ABSTRACT

Context. The Gaia mission has delivered hundreds of thousands of variable star light curves in multiple wavelengths. Recent work demonstrates that these light curves can be used to identify (non-)radial pulsations in the OBAF-type stars, despite the irregular cadence and low light curve precision of order a few mmag. With the considerably more precise TESS photometry, we revisit these candidate pulsators to conclusively ascertain the nature of their variability.

Aims. We seek to re-classify the Gaia light curves with the first two years of TESS photometry for a sample of 58,970 p- and g-mode pulsators, encompassing γ Dor, δ Scuti, SPB, and β Cep variables. From the TESS data, we seek to assess the quality of Gaia's classification of non-radial pulsators which is based on sparse, years-long light curves of mmag precision. We also supply four new catalogues containing the confirmed pulsators, along with their dominant and secondary pulsation frequencies, the number of independent mode frequencies, and a ranking according to their usefulness for future asteroseismic ensemble analysis.

Methods. We first analyze the TESS light curves independent of their Gaia classification by prewhitening all dominant pulsation modes down to a 1% false alarm probability. Using this, in combination with a feature-based random forest classifier, we identify different variability types across the sample.

Results. We find that the Gaia photometry is exceptionally accurate for detecting the dominant and secondary frequencies, reaching approximately 80% accuracy in frequency for p- and g-mode pulsators. The majority of Gaia classifications are consistent with the classifications from the TESS data, illustrating the power of the low-cadence Gaia photometry for pulsation studies. We find that the sample of g-mode pulsators forms a continuous group of variable stars along the main sequence across B, A, and F spectral types, implying that the mode excitation mechanisms for all these pulsators need to be updated with improved physics. Finally, we provide a rank-ordered table of pulsators according to their asteroseismic potential for follow-up studies, based on the number of sectors they have been observed in, their classification probability, and the number of independent modes found in the TESS light curves from the nominal mission.

Conclusions. Our catalogue offers a major increase in the number of confirmed gravity-mode pulsators with an identified dominant mode suitable for follow-up TESS ensemble asteroseismology of such stars.

Key words. Techniques: photometric – Stars: Rotation – Stars: binaries: general – Stars: oscillations (including pulsations) – Methods: statistical – Catalogs

1. Introduction

Over the course of the past century, variable stars have proven to be an invaluable resource in the refinement of our understanding of stellar structure and evolution. This has become notably apparent following the advent of high-precision space photometry, a revolution which has provided astronomers with a continuous stream of high-frequency micro-magnitude precision light curves spanning the entirety of the Hertzsprung-Russell diagram (HRD, Kurtz 2022). The richness of this data has paved the way for advanced asteroseismic investigations into the internal structure of stars (Aerts 2021).

Asteroseismic modelling has been utilized for thousands of red giants, with stochastically excited identified modes exhibiting amplitudes around 0.1 mmag and periodicities on the order of hours (e.g., Hekker & Christensen-Dalsgaard 2017, for

a review). Conversely, the sample of uniformly analysed white dwarf successors to these red giants only includes a few tens of compact pulsators with identified modes (e.g. Hermes et al. 2017). Despite the possibility of their amplitudes reaching several mmag, the limited sample size of DAV and DBV white dwarf pulsators is primarily due to their characteristics as faint, fast gravity-mode pulsators (e.g. Córscico et al. 2019, for a summary). Therefore, monitoring these pulsators for asteroseismology necessitates a cadence under a minute, as opposed to the half-hour cadences suitable for covering the hours-long periodicities of red giant modes.

Asteroseismology of main sequence pulsators has so far also only been applied to limited ensembles compared to red giants. For low-mass dwarfs like the Sun this limitation is due to the low amplitudes (of order $10 \mu\text{mag}$) and short periods (of order minutes) of their solar-like pulsations (García & Ballot 2019, for a

arXiv:2405.01539v2 [astro-ph.SR] 7 Jun 2024

review). For intermediate- and high-mass dwarfs the limitations are mainly caused by the fast rotation (see [Aerts & Tkachenko 2024](#), for a review), preventing identification of the asymmetrically split merged mode multiplets for the majority of discovered class members. So far, homogeneous asteroseismic modelling of intermediate-mass dwarfs, treating all pulsators in the same way has only been done for a few modest ensembles:

- 60 young unevolved δ Scuti stars very close to the zero-age main sequence with high-frequency pressure modes ([Bedding et al. 2020](#)). As for most of the slowly rotating red giant pulsators, their modelling was done while ignoring the Coriolis force and relied on just the large frequency separation and the frequency of maximum power ([Panda et al. 2024](#)), rather than the fitting of individual mode frequencies;
- 26 slowly pulsating B stars (SPB stars, [Pedersen et al. 2021](#)) whose individual identified mode frequencies were modelled based on the methodological framework designed specifically for gravito-inertial modes in fast rotators relying on the Traditional Approximation of Rotation (TAR), as developed in [Aerts et al. \(2018\)](#), to which we refer for details);
- 490 γ Doradus (γ Dor) stars whose measured buoyancy travel time and near-core rotation frequency deduced from identified gravito-inertial modes adopting the TAR were modelled by [Mombarg et al. \(2024\)](#); 37 of these γ Dor stars had their individual modes modelled by methodology based on the TAR coupled to a neural network ([Mombarg et al. 2021](#)).

For the high-mass β Cep stars, homogeneous ensemble modelling of their few (typically between 3 and 5) identified pressure modes has not yet been done; [Bowman \(2020\)](#) summarised some of the results for seven individual class members. Clearly, ensemble asteroseismology of intermediate- and high-mass dwarfs is still in its early stages, despite the discovery of thousands of class members ([Handler et al. 2019](#); [Burssens et al. 2023](#); [Eze & Handler 2024](#)). Lack of mode identification prevents applications to large ensembles. Novel approaches to filter thousands of main-sequence pulsators with proper mode identification are therefore in order. The initial attempts for the toughest case of gravito-inertial pulsators by [Garcia et al. \(2022a,b\)](#) based on just the first year of TESS monitoring already illustrated the major potential of this mission for ensemble asteroseismology of fast rotators across the Milky Way, in line with the opportunities discussed in [Aerts & Tkachenko \(2024\)](#).

The current study aims to increase the sample of main sequence pulsators of spectral types O, B, A, and F (hereafter OBAF pulsators) with the potential for ensemble asteroseismology with an order of magnitude. Our work is focused on the availability of homogeneously assembled seismic and non-seismic observables. Even if it was not designed for this type of research, the ESA Gaia mission ([Gaia Collaboration et al. 2016b,a](#)) has a significant role to play in this context. We tackle the challenging search for suitable large ensembles of dwarf pulsators by screening the homogeneous database of stellar properties and sparse time-series photometry offered by Gaia’s Data Release 3 (DR3, [Gaia Collaboration et al. 2023b](#)). Starting from the sample of 106,207 candidate OBAF pulsators classified by [Gaia Collaboration et al. \(2023a\)](#), we analyse those targets among this large ensemble having high-cadence high-precision light curves assembled by the NASA TESS space telescope ([Ricker et al. 2015](#)).

In order to prepare the ‘industrialisation’ of asteroseismic ensemble modelling of OBAF pulsators, we need to find targets

with tens of identified modes from the TESS photometry among the ‘zoo of variables’ along the main sequence ([Eyer et al. 2023](#)). Thousands of variable intermediate- and high-mass dwarfs have already been found from high-cadence uninterrupted space photometry (e.g., [Uytterhoeven et al. 2011](#); [Balona et al. 2011a](#); [Balona & Dziembowski 2011](#); [Balona et al. 2011b](#); [Balona 2016](#); [Balona et al. 2019](#); [Antoci et al. 2019](#); [Pedersen et al. 2019](#); [Burssens et al. 2019, 2020](#)). Their variability is caused by different physical phenomena, making identification of the pulsation modes for large ensembles of OBAF pulsators a major obstacle. In this era of high-cadence space photometry the variability phenomena are better understood and include stellar flaring (e.g. [Balona 2015](#); [Pedersen et al. 2017](#)) along with other magnetic variability (e.g. [Shultz et al. 2019](#); [David-Uraz et al. 2019](#); [Sikora et al. 2019a](#)), rotational modulation (e.g., [Bowman et al. 2018](#); [Sikora et al. 2019b](#)), low-frequency variability interpreted in terms of internal gravity waves (e.g., [Aerts & Rogers 2015](#); [Bowman et al. 2019, 2020](#)) or subsurface convection (e.g., [Cantiello & Braithwaite 2019](#); [Cantiello et al. 2021](#)), eclipses in close binaries (e.g., [Kirk et al. 2016](#); [Ijspeert et al. 2021](#)) and so on. This non-exhaustive list of variable phenomena often occurs in combination with nonradial pulsations (as summarised in [Kurtz 2022](#)).

Furthermore, it has long been established that OBAF pulsators coexist with various types of variable stars along the main sequence in the Hertzsprung-Russell diagram (HRD) (e.g., [Briquet et al. 2007](#)). The recently released Gaia Data Release 3 (Gaia DR3) data reaffirm this observation, demonstrating that the classes of variability, including OBAF pulsators, encompass a substantial proportion of stars distributed across nearly the entire main sequence within the intermediate- and high-mass dwarf star population ([Gaia Collaboration et al. 2023a](#)). This phenomenon is further substantiated by investigations of young open clusters, which have been systematically monitored through joint efforts involving the Gaia mission, as well as the refurbished *Kepler* (known as K2) and Transiting Exoplanet Survey Satellite (TESS) missions (e.g., [White et al. 2017](#); [Murphy et al. 2022](#); [Bedding et al. 2023](#); [Fritzewski et al. 2024](#); [Li et al. 2024](#)). Consequently, it is prudent to adopt an approach that involves scrutinizing the time-series photometric data itself, rather than solely focusing on the stellar positions within the HRD, to effectively address our scientific objectives. Gaia DR3 provides us with the requisite data to pursue this approach in our quest to identify the most appropriate ensembles of OBAF pulsators.

In this paper, we revisit a large fraction of the 106207 OBAF pulsators discovered in the sparse Gaia DR3 photometry by [Gaia Collaboration et al. \(2023a\)](#) with the goal to derive and analyse their TESS light curves. We focus on the poorly populated samples of nonradial pulsators having the highest asteroseismic potential and thus revisit the candidate γ Dor stars, Slowly pulsating B (SPB) stars, β Cep stars, and δ Scuti stars identified by [Gaia Collaboration et al. \(2023a\)](#). The γ Dor and SPB g-mode pulsators have been revisited already by [Aerts et al. \(2023\)](#) in terms of their astrophysical properties, but the β Cep and δ Scuti p-mode pulsators have not been evaluated as such. Here, we confront the Gaia DR3 variability properties for the members assigned to these four classes with their TESS data when available. Our work has the following two major aims:

- to assess the quality of Gaia’s classification of nonradial pulsators, which is only based on sparse years-long light curves of mmag precision, by confronting its outcome with high-cadence μ mag precision TESS space photometry for all class

members that have Gaia and TESS independent data sets in the public domain;

- to create four large new catalogues containing Gaia-discovered nonradial pulsators confirmed by TESS, offering the community their TESS light curves covering the first year of monitoring, their independent mode frequencies, and identification of the dominant mode if possible. These catalogues are an optimal starting point for future ensemble asteroseismic modelling.

2. Gaia and TESS Data

2.1. The four samples of candidate pulsators

Our samples consist of the p- and g-mode pulsators discussed in [Gaia Collaboration et al. \(2023a\)](#). For the g-mode pulsators, we take the 15,062 candidates from [Aerts et al. \(2023\)](#). This sample contains 11,636 γ Dor and 3,462 SPB star candidates. In addition, we consider the 222 candidate β Cep stars and 85,317 δ Scuti candidates classified as such by [Gaia Collaboration et al. \(2023a\)](#). For the latter two classes, the extra vetting based on the expected frequency range as done for the g-mode pulsators by [Aerts et al. \(2023\)](#) is not meaningful, because their dominant p-mode frequencies are expected to intervene with (multiples of) Gaia’s main satellite frequency near 4 d^{-1} at mmag level. Moreover, large fractions among the β Cep and δ Scuti stars may have a dominant high-amplitude radial mode, so a restriction on amplitude as extra vetting rule as adopted by [Aerts et al. \(2023\)](#) for the γ Dor and SPB pulsators is less obvious to define for the p-mode pulsators.

To construct the four samples for the current work, we cross-match their Gaia Data Release 2 (DR2, [Gaia Collaboration et al. 2018](#)) identifications (IDs) using the ‘nearest neighbours’ table. To obtain their TESS IDs, we then cross-match the Gaia DR2 IDs against the TESS Input Catalog (TIC, [Stassun et al. 2018](#)). The final cross-matched sample among DR3 ([Gaia Collaboration et al. 2023b](#)), DR2, and TIC contains 85,313 δ Scuti stars, 11,636 γ Dor stars, 3,426 SPB stars, and 222 β Cep stars. The loss of several stars in the cross-matching process is a result of the DR2 to DR3 best neighbours matching catalogue, which is not strictly one-to-one.

2.2. TESS photometry

The majority of the sample has not been targeted for dedicated observations by TESS. With no official light curves delivered by the TESS team using the SPOC pipeline, we instead use light curves from the TESS Gaia light curve (TGLC) catalogue, produced from full-frame images by [Han & Brandt \(2023\)](#). TGLC light curves were used as an alternative to the Quick-Look Pipeline (QLP, [Huang et al. \(2020\)](#)) because they reach fainter than 13.5 mag. The TGLC light curves leverage Gaia photometry and astrometry to inform light curve extraction by building a local point spread function forward model, making it a viable source for fainter stars, where Gaia astrometry is useful for resolving contaminated stars.

We use the TGLC light curves from the first 26 sectors of the TESS mission calculated by the TGLC pipeline from the full-frame images. These light curves are at a nominal 30-minute cadence. We use the calibrated aperture flux with the “good” quality flags. For each light curve, we perform 3σ clipping of the flux and apply a Gaussian filter with a standard deviation of 100

to remove significant long-term trends. A table containing the curl scripts used to download the data is available in electronic format as supplementary material. The TGLC light curves are available in the first 26 TESS sectors for 45,919 δ Scuti stars, 10,099 γ Doradus stars, 2,777 SPB stars, and 175 β Cep stars, leading to a total analysis sample of 58,970 variables out of the original target list.

3. Confrontation between the two light curves per sample star

3.1. Prewhitening of dominant pulsation modes

To analyze the candidate pulsators in our sample we have developed an automated prewhitening scheme based on the approach used for p-mode pulsators in [Hey et al. \(2021\)](#), with several modifications. The algorithm functions as follows: it begins by identifying the highest peak in the amplitude spectrum. It then optimises the value of the peak frequency from a sinusoidal function in the time domain characterized by a frequency, amplitude, and phase. This fitted sinusoid is then subtracted from the light curve, repeating iteratively until a predefined stopping condition. In contrast to [Hey et al. \(2021\)](#) where the stopping condition was the signal-to-noise ratio (SNR) of the peak, our method employs the false-alarm level for the highest amplitude peak, ensuring it falls below a 1% probability threshold. If this condition is met, the peak is deemed significant, removed, and the prewhitening process continues.

The prewhitening procedure is applied to each peak exceeding the 1% significance level in the amplitude spectrum, or until a maximum of 100 iterations is reached, whichever occurs first. Additionally, for each peak, we calculate its ‘prominence’, which quantifies the peak’s distinctiveness relative to the surrounding amplitude spectrum. This metric serves as a useful diagnostic tool for evaluating individual modes, especially in the scenario where a single prewhitening step does not completely remove a peak (a common occurrence in non-sinusoidal signals).

We perform the prewhitening for all stars in our sample. Stars with more than one sector of TESS observations are stitched together prior to prewhitening, with each sector having a simple 5σ outlier removal and long-term trend removal with a Gaussian filter. During the prewhitening routine, it is common to encounter combination frequencies ([Kurtz et al. 2015](#)). These can be identified and subsequently removed using the following equation ([Li et al. 2019](#)):

$$|f_k - (n_i f_i + n_j f_j)| < \epsilon; \quad (1)$$

where i , j , and k are indices of the frequency peaks, f_i and f_j are the parent frequencies, f_k is the candidate for the combination frequency, n_i and n_j are combination coefficients, and ϵ is the threshold for identification. Following the approach of [Li et al. \(2019\)](#), we limit our analysis to the 20 highest amplitude peaks, considering them as potential parent frequencies. Our criterion for combinations is restricted to cases where $|n_i| + |n_j| \leq 2$. In light of the TESS data’s lower precision compared to the *Kepler* data, we opt for a considerably larger ϵ value of 0.002 d^{-1} , compared to that used by [Li et al. \(2019\)](#). We also remove harmonics, defined as integer or half-integer multiples of the parent frequency. Such harmonics are common, for example, in eclipsing binary samples (e.g., [IJSpeert et al. 2024](#)).

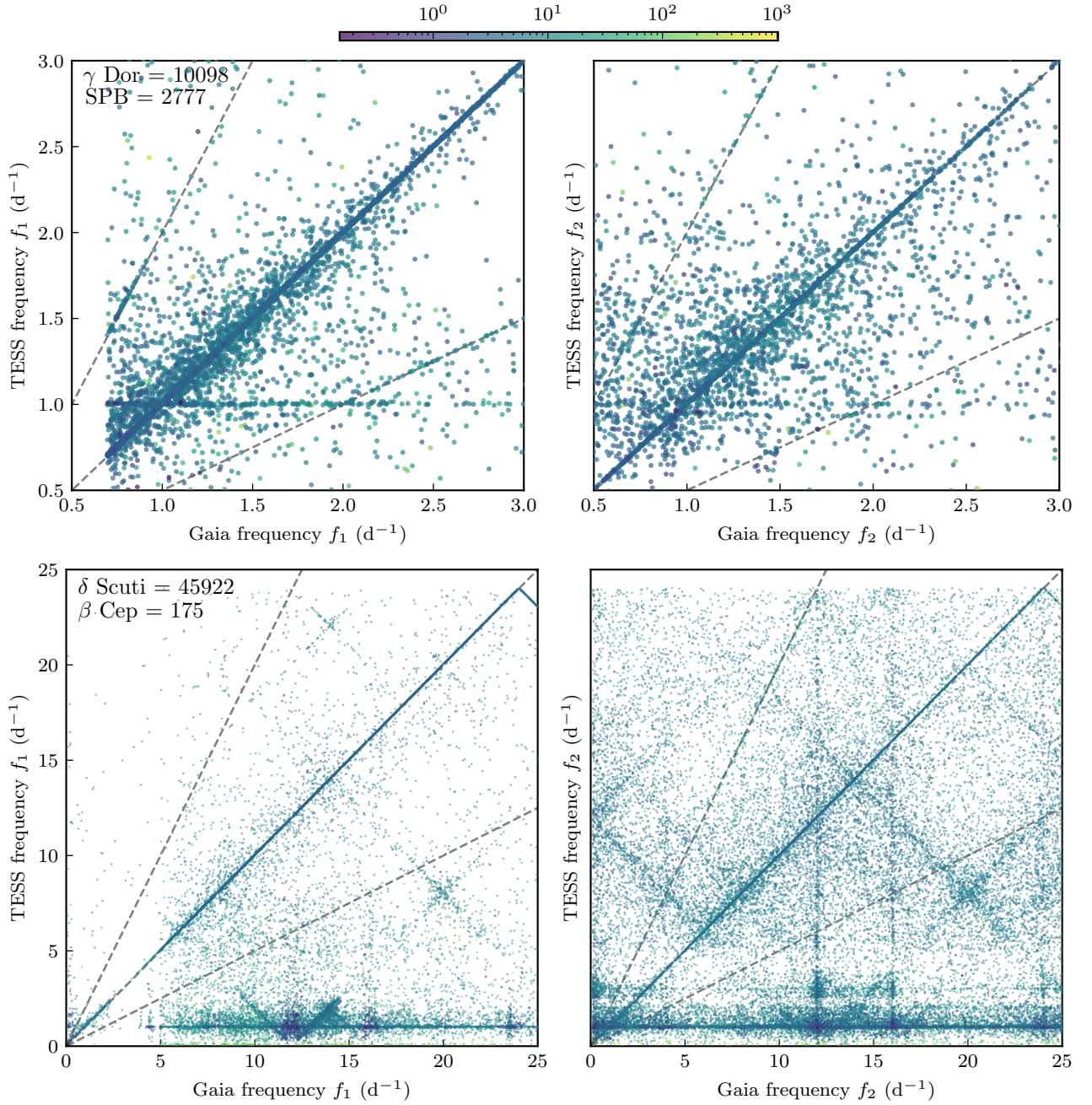


Fig. 1. Left: Comparison of measured dominant TESS frequency against *Gaia* frequency for the g-mode pulsators (top) and p-mode pulsators (bottom), colored by the amplitude of the variability (ppt). Right: The same for the secondary frequency. The dashed lines indicate the half, unity, and twice relationships among the frequencies. We compare the sample of g-mode candidate pulsators before removing combination frequencies, to match the method of [Aerts et al. \(2023\)](#). The criss-cross structures in the p-mode plots are caused by aliases of the true signal around the Nyquist limit.

3.2. Comparison of the two dominant frequencies

Here we compare the results of our TESS light curves against the *Gaia* photometry explored in [Gaia Collaboration et al. \(2023a\)](#) and [Aerts et al. \(2023\)](#). Figure 1 shows the comparison between dominant and secondary modes between the TESS and *Gaia* data for all the candidate pulsators in the four samples, grouping the p-mode and g-mode pulsators in separate panels. The agreement is particularly good considering the sparse sampling of the *Gaia* data, with 69% of the sample lying along the bisector with a 0.1 d^{-1} tolerance for the dominant frequencies of the p-modes,

and 80% for the g-mode frequencies. This result on comparisons between the dominant frequencies in the *Gaia* and TESS light curves is superior to the 20% agreement in dominant frequency between the *Gaia* and *Kepler* light curves for the few tens of γ Dor and SPB stars found by [Gaia Collaboration et al. \(2023a\)](#), see their Appendix A).

There is a clear systematic in the TGLC light curves at 1 d^{-1} caused by what we believe to be reflected light from Earth ('earthshine'). We find no correlation between the amplitude of this signal and whether the star falls along a TESS bisector or not. For the p-mode pulsators, Fig. 1 reveals additional

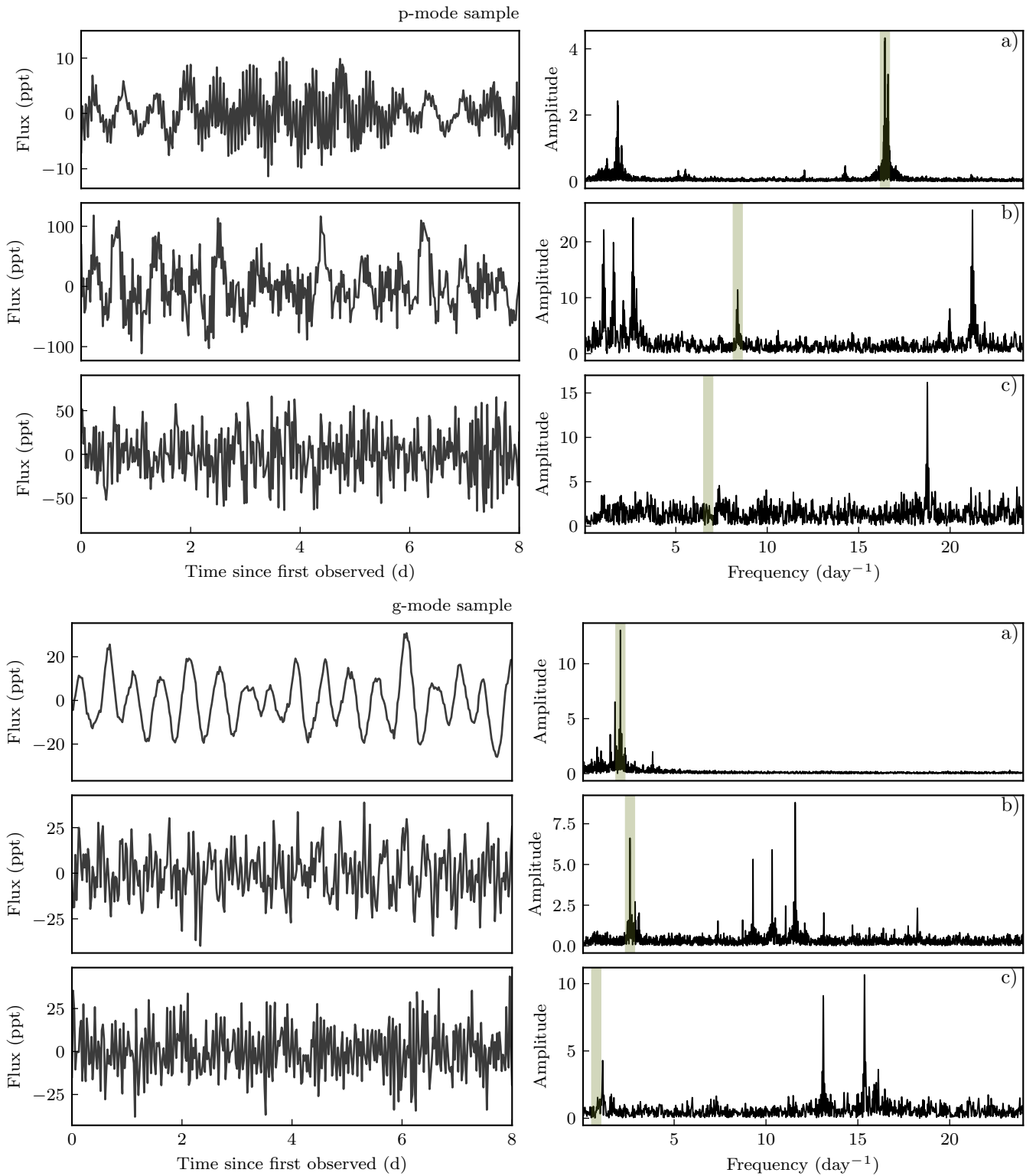


Fig. 2. Example light curves and amplitude spectra from the p-mode (top three panels) and g-mode (bottom three panels) candidate sample. The green vertical line marks the measured Gaia frequency. We show the following cases; a) where the measured Gaia frequency is in good agreement with TESS, b) where the measured Gaia frequency is not the true dominant one, and c) the measured Gaia frequency is incorrect.

criss-crossing structures aside from the 1 d^{-1} systematic in the TESS data. This phenomenon is understood in terms of the 30-min sampling by TESS, causing a mirroring effect around the Nyquist frequency that leads to an aliased signal of the true frequency. For example, a δ Scuti variable with a true pulsation at

44 d^{-1} will have an indistinguishable copy of the signal appearing at around 4 d^{-1} if observed in 30-minute cadence. This effect can be seen, for example, in the δ Scuti and rapidly oscillating Ap stars observed by *Kepler* in long-cadence (Bell et al. 2017; Murphy et al. 2019; Hey et al. 2019). The clustering of modes

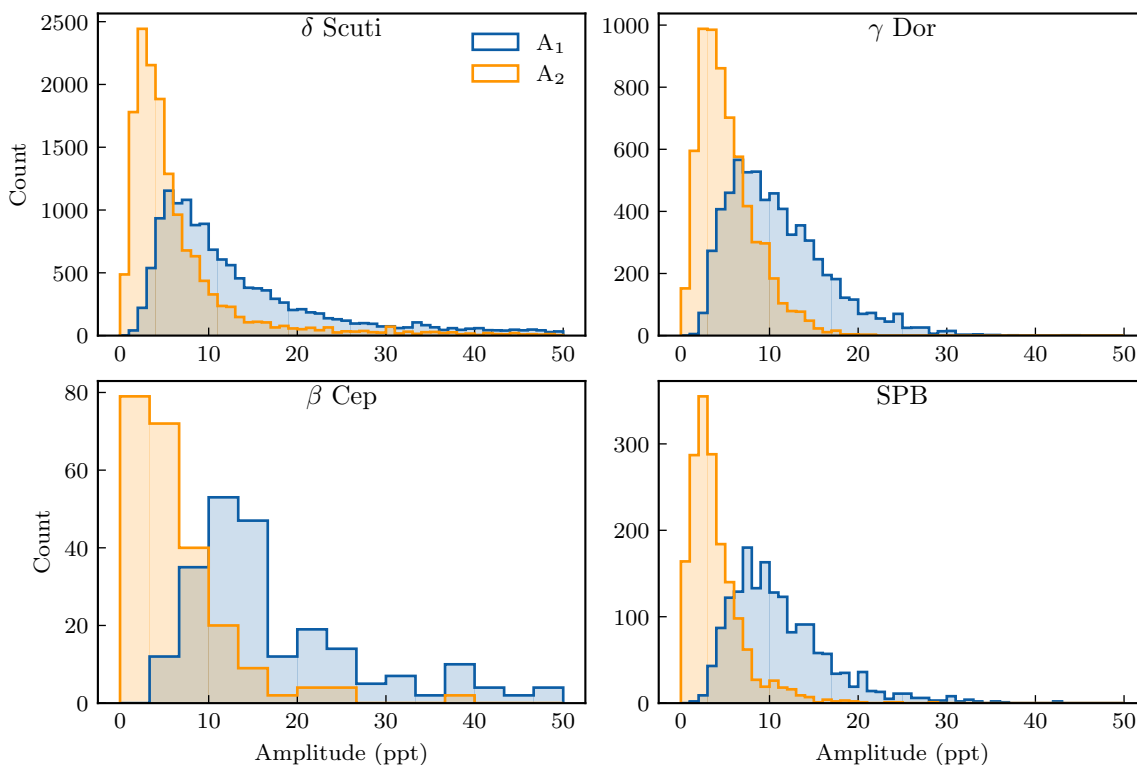


Fig. 3. Distribution of amplitudes for the dominant (blue) and secondary (orange) frequencies for each variable type in our sample. Note that we use only stars where the dominant frequency lies on the bisector within 0.1 d^{-1} tolerance for the TESS/Gaia overlap (cf. Fig. 1).

around $10\text{-}15 \text{ d}^{-1}$ are likely aliases of the true δ Scuti p-mode oscillations that are expected to peak above the Nyquist limit Hey et al. (2021). Note that the true and aliased signals of coherent pulsators can be distinguished in the *Kepler* data as a consequence of periodic modulation of the light curve measurement times (Murphy et al. 2013).

We show a series of light curves in Fig. 2 to demonstrate pathological cases of the Gaia and TESS data. For the p- and g-mode candidate sample, we illustrate three occurring scenarios: a) the Gaia measured dominant frequency is correct and confirmed by TESS, b) Gaia picks up a secondary peak of an otherwise correctly classified pulsator, and c) the dominant Gaia frequency is wrong and likely of instrumental origin. The latter situation calls for a re-evaluation of the Gaia DR3 variability classification of the star, based on its TESS light curves. We tackle this subject in Sect. 4. We also note that the Gaia identification of dominant and secondary frequencies is dependent on the scanning law (Steen et al. 2024).

Figure 3 shows the histograms of the primary and secondary amplitudes for the TESS data of each variable type, where the dominant frequency is in good (that is, to within 0.1 d^{-1}) agreement with the measured Gaia frequency, and the classification is accurate in both TESS and Gaia with a classification probability > 0.5 (Section 4). We perform a two-sided Kolmogorov-Smirnov test to compare the amplitude distributions across each of the two variability classes with the same type of modes. The null hypothesis for this test is that the two distributions are identical. That is, they are drawn from the same underlying distribution. We choose a confidence level of 95% for the test, such that the null hypothesis is rejected if the p-value is less than 0.05.

For the δ Scuti and β Cep sample, the test indicates that their amplitude distributions are statistically different, with a p-value of around 10^{-14} . This result can be understood from various arguments. First, the two classes of p-mode pulsators are subject to the same type of excitation mechanism, namely the opacity (or κ) mechanism, but it acts in a different layer in the outer envelope of the star. For the β Cep stars it concerns the partial ionisation zone of iron-like isotopes occurring at a temperature of about 200kK , while the heat engine in the case of δ Scuti stars is mainly acting in the cooler second ionization zone of helium located in the region with a temperature of about 45kK , with a small contribution from the even cooler hydrogen ionization zone as well (Pamyatnykh 1999; Guzik 2021). Moreover, in the β Cep stars the excitation layer is situated within a fully radiative envelope, while the δ Scuti stars have a thin outer convective envelope where proper treatment of time-dependent convection is required to perform the mode calculations (Dupret et al. 2005b). These different zones have different local time scales and hence lead to different mode periodicities and amplitudes. The wave damping is also different in the outer layers of both types of pulsators. Finally, unlike for the β Cep stars, strong amplitude modulation occurs in many δ Scuti stars (Bowman et al. 2016).

For the γ Dor and SPB sample, however, we find that the null hypothesis can not be rejected with a p-value of 0.055. This indicates that the distributions of their amplitudes are statistically the same. From the observational side, this is expected from prior work based on variability classification – only colour information allows us to distinguish between the SPB and γ Dor classes from photometric data (Audenaert et al. 2021), and even then, there is still confusion for stars with an effective temperature between $8500\text{-}9500 \text{ K}$ (Aerts et al. 2023). The mode frequency ranges for both types of pulsators are roughly the same, as are

the ranges of the overtones of the excited modes (Li et al. 2020; Pedersen et al. 2021) and of the internal rotation rates when expressed in terms of the critical break-up frequency (Van Reeth et al. 2016, 2018; Pedersen 2022a). The equal amplitude distributions among γ Dor and SPB stars are a natural consequence of the known mode excitation mechanisms for the two classes of pulsators. While the SPB stars have their g modes excited by the κ mechanism acting in the same partial ionisation zone of iron-like isotopes as the modes in the β Cep stars (Pamyatnykh 1999; Townsend 2005; Szweczek & Daszyńska-Daszkiewicz 2017), the γ Dor stars are subject to at least two not mutually exclusive excitation mechanisms: while the κ -mechanism comes into play for the hottest class members, the dominant excitation is caused by flux blocking at the base of the thin outer convective envelope. This base is situated in a region with temperatures between roughly 200 kK and 500 kK (Guzik et al. 2000; Dupret et al. 2005a; Bouabid et al. 2013) and explains the similarity of the mode frequencies and amplitudes for SPB and γ Dor stars.

With our work, we re-affirm that the current excitation predictions cannot be complete as we observe more modes than predicted and they occur also in stars outside the currently available instability strips. This was found from the Gaia DR3 results in Gaia Collaboration et al. (2023a) and already independently found and confirmed from *Kepler* and TESS space photometry (cf. the recent assembly and summary by Balona 2024). Fritzewski et al. (2024) and Mombarg et al. (2024) found the majority of the observed *Kepler* γ Dor stars to have a mass above $1.5 M_{\odot}$ and many of them to be hotter than the blue edge of current γ Dor instability strips, well into the δ Scuti classical instability strip and even above it. One promising route to achieve extra mode excitation in addition to the known mechanisms active in SPB and γ Dor stars is nonlinear mode coupling, which was already established in large-amplitude SPB stars (Van Beeck et al. 2021). This mechanism may excite extra modes via energy exchange between modes, aside from the self-driven linear modes due to the κ mechanism. While a similar study on nonlinear mode coupling has not yet been done for γ Dor stars, their *Kepler* light curves show similar cusp-like shapes near the maxima than the SPB stars with nonlinear mode coupling do (cf. compare the data in Van Reeth et al. 2015; Pedersen et al. 2021).

Finally, it has been shown that adding novel physical ingredients in mode excitation computations may appreciably enlarge the instability strips, such as the Coriolis force due to fast rotation (Bouabid et al. 2013; Szweczek & Daszyńska-Daszkiewicz 2017) and radiative levitation due to atomic diffusion (Deal et al. 2016; Rehm et al. 2024). All of this makes comparing observational instability strips from surveys of pulsators with predicted strips based on just one choice of input physics of limited value. This was already highlighted from the dominant frequencies found in the Gaia DR3 light curves of g-mode pulsators in Gaia Collaboration et al. (2023a), got stressed again in the review on asteroseismology of fast rotators by Aerts & Tkachenko (2024), and is reinforced here from our indistinguishable TESS amplitude distributions for the γ Dor and SPB classes shown in Fig. 3. It is for this reason that we merge the SPB and γ Dor classes in Sec. 4.

3.3. Gaia amplitude ratios

So far we worked with the Gaia G passband. It covers the wavelengths between 330 nm to 1050 nm, with peak sensitivity at

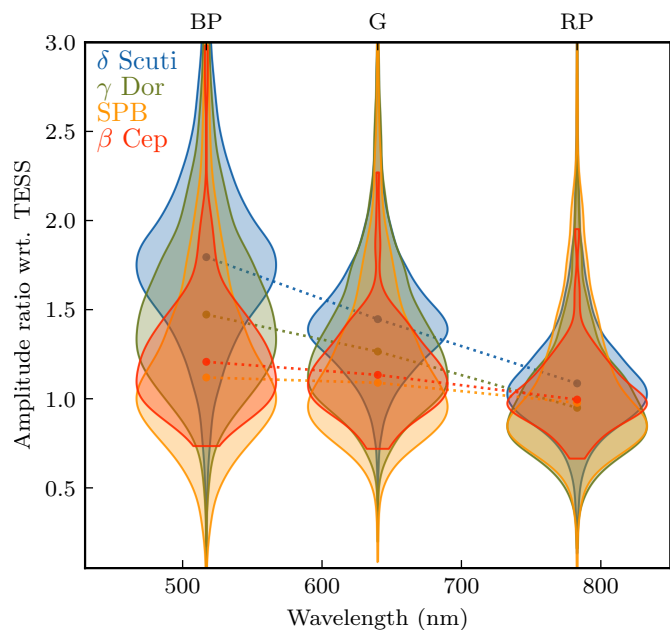


Fig. 4. Violin plot of the amplitude ratios for the four samples deduced from the light curves in the three Gaia bandpasses with respect to the amplitude in the TESS band (covering approximately 600 - 1,000 nm). The shaded regions indicate the density distributions for each of the samples, with the solid points showing the median. For clarity, we do not add the density distribution centred around value 1.0 for the TESS bandpass itself.

640 nm. But DR3 also delivered the light curves in the RP and BP colour bands. In practice, these BP and RP bands are blue and red cuts of the broad G band, covering the ranges from 330 nm to 680 nm (BP) and from 630 nm to 1050 nm (RP), with maximum responses at 517 nm and 783 nm, respectively (Weiler 2018). On the other hand, the TESS detector passband spans from 600 nm to 1000 nm with central wavelength at 787 nm (Ricker et al. 2015).

Having time series data with colour information is advantageous for asteroseismology in the case of ambiguous mode identification in terms of the spherical harmonic wavenumbers (l, m) characterising the geometry of the mode. Indeed, the theoretical expression for the observed amplitudes of a mode described by the spherical harmonic function Y_l^m and viewed upon at an inclination angle i depends on the wavelength, via the perturbations of the atmospheric flux and limb darkening caused by the mode (see Eq. (6.29) in Aerts et al. 2010). The dependencies of this expression on the azimuthal order m and on the inclination angle i of the star's pulsation symmetry axis drop out of the expression of amplitude ratios for different wavelengths. This is why observed amplitude ratios deduced for light curves observed in different passbands have been used to identify the mode degree l of main-sequence pulsators (e.g., Heynderickx et al. 1994; Breger 2000; Dupret et al. 2003; Aerts et al. 2004; De Cat 2017; Brunsten et al. 2018). All these applications of mode identification assumed one fixed set of input physics for the theoretical predictions. We now know from space asteroseismology that this is not appropriate for such pulsators (Aerts 2021; Johnston 2021; Pedersen 2022b).

Although the Coriolis and centrifugal forces complicate this capacity of mode identification in fast rotators such as δ Scuti stars (Daszyńska-Daszkiewicz et al. 2002) and SPB stars

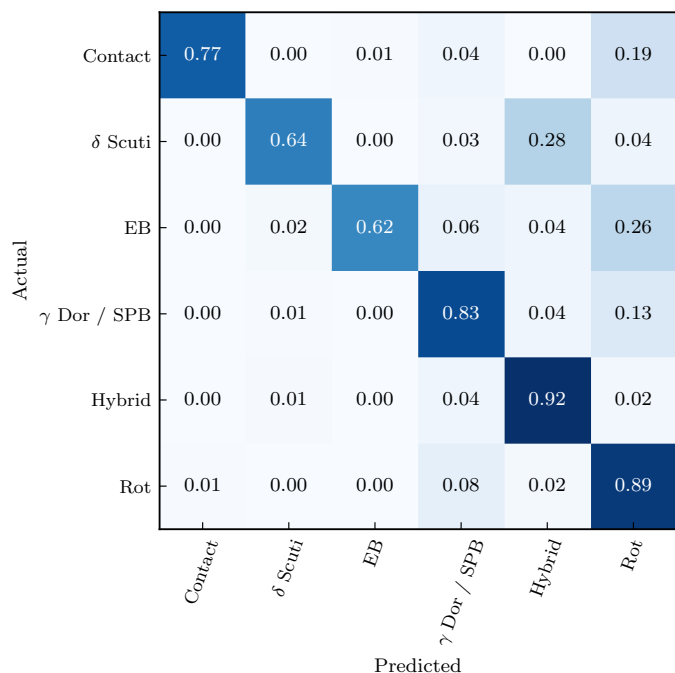


Fig. 5. Confusion matrix for the Random Forest classifier normalized against the true values. Here, hybrid refers to the simultaneous presence of δ Scuti p-mode pulsations and γ Dor or SPB g-mode pulsations.

(Townsend 2003), we have a good understanding of how they do so. Therefore, it was recently suggested by Aerts & Tkachenko (2024) to exploit amplitude ratios for stars whose identification of (l, m) is already established. Indeed, in this case, any diversity in observed amplitude ratios encapsulates differences in the internal, atmospheric, and limb-darkening physics of the star. Figure 11 in Aerts & Tkachenko (2024) illustrates this (future) potential opportunity from measured amplitude ratios of prograde dipole gravito-inertial modes observed in both Gaia and *Kepler* data of 23 γ Dor stars. Here, we illustrate the potential of amplitude ratios from combined Gaia and TESS light curves for the four samples of new Gaia DR3 pulsators.

For all the stars with consistent dominant frequency and consistent classification (Section 4) in the Gaia G and TESS passbands, we computed the ratios of the G, BP, and RP amplitudes of that frequency with respect to the amplitude in the TESS passband. We show a violin plot of the results for the four classes in Fig. 4. This figure is in line with expectations for low-degree ($l \leq 2$) mode behaviour in stars with slow to moderate rotation, whose ratios are predicted to decrease with increasing wavelength for the three Gaia passbands (e.g., Heynderickx et al. 1994; De Ridder et al. 2004). Comparison between Fig. 11 in Aerts & Tkachenko (2024) and the violin plot in Fig. 4 illustrates the superiority of TESS over *Kepler* for this type of exploratory research based on the dominant pulsation mode, given that the TESS pulsators are generally much brighter than the *Kepler* γ Dor stars, leading to more precise amplitude ratios. Given its potential for asteroseismology, we provide the Gaia amplitude ratios alongside the database of prewhitened modes as supplementary data.

Table 1. Classifications of the p- and g-mode candidate sample. The full table in electronic format, with probabilities for each class, is available online.

DR3 Source ID	Sector	Class	Probability
2070667440659268352	14	δ Scuti	0.26
2247307763228746240	14	Hybrid	0.67
5311721917688649856	10	δ Scuti	0.35
5617799085534387968	7	δ Scuti	0.67
5657691905702501888	9	γ Dor/SPB	0.93
		\vdots	
2925330438953873024	7	Hybrid	0.95
2164506978535115776	16	Hybrid	0.41
5516571310575369472	8	δ Scuti	0.74
5964132569560169472	12	δ Scuti	0.57
5661189937524776320	9	γ Dor/SPB	0.90

4. Re-classification of the pulsators from TESS

We now re-evaluate the Gaia DR3 variability classification from Gaia Collaboration et al. (2023a) by relying on the highly sampled and more precise TESS light curves.

4.1. Training sample

To distinguish between various classes of variability, in particular, intrinsic and extrinsic variability, we have implemented a simple feature-based Random Forest classifier, similar to Aude-naert et al. (2021) and Barbara et al. (2022). This classifier seeks to identify different types of variability based on extracted singular value features of the light curve. These features, calculated with `pySCHEM22` (Lubba et al. 2019), are spread across different categories concerning linear autocorrelation and periodicity of the flux, extreme events, distributions that ignore time ordering, and more. These features have been chosen such that they are minimally redundant and capture the largest possible variance of the input time series.

Our training sample for the classifier is sourced from both *Kepler* and TESS. For *Kepler*, we use the sample compiled by Barbara et al. (2022), which consists of high-level variability classifications pertaining to A/F-type stars, including contact and detached binaries, δ Scuti stars, γ Dor stars, RR Lyrae variables, along with rotational and non-variables. Given that this sample relies heavily on data derived from the *Kepler* mission, it poses certain challenges when applied to classify TESS data; the majority of the stars within the sample are of such faint magnitude that their variability signal cannot be observed within the TESS data, hence directly comparing the TESS light curves with the *Kepler* labels is not feasible. As an alternative, we have devised a strategy where we modify the *Kepler* light curves to mirror the single-sector observations of the TESS photometry. The modifications we have implemented on the *Kepler* light curves are as follows; limiting the time span to a duration of less than 27 days, adding noise proportional to the magnitude of the star, and introducing a data gap at 13.7 days to simulate the TESS downlink.

We further construct a TESS training sample compiled against a series of A/F variability papers (Skarka et al. 2022; Sikora et al. 2019a; Garcia et al. 2022a,b; Shi et al. 2023), focusing on either the classification of A/F stars or targeting a specific variable type in TESS. The Skarka sample consists of variable A/F stars in the Northern continuous viewing zone, the Sikora

Table 2. Results of classification for each sample, showing the breakdown of individual classifications as a fraction of the total sample. The number in brackets represents the fraction of the sample for the class.

γ Dor (N=10,047)	γ Dor / SPB	6,489 (0.65)
	Rotation	2,416 (0.24)
	Hybrid	618 (0.06)
	Eclipsing binary	251 (0.02)
	Contact binary	205 (0.02)
	δ Scuti	58 (~ 0)
δ Scuti (N=45,648)	δ Scuti	19,226 (0.42)
	Hybrid	15,395 (0.34)
	Rotation	4,371 (0.10)
	Eclipsing binary	3,656 (0.08)
	γ Dor / SPB	2,962 (0.06)
	Contact binary	38 (~ 0)
SPB (N=2,795)	γ Dor / SPB	1,481 (0.53)
	Rotation	948 (0.34)
	Hybrid	209 (0.07)
	Eclipsing binary	88 (0.03)
	Contact binary	59 (0.02)
	δ Scuti	10 (~ 0)

sample contains rotationally variable A-type stars, the Garcia sample contains 60 γ Dor stars with a long observational baseline, and the Shi sample contains 286 SPB stars.

Each sample contains a slightly different type of classification, which we homogenize into new categories. In particular, we merge all the ellipsoidal and semi-detached binaries into the “contact” class, leaving the eclipsing binary (EB) class for purely detached cases. We also merge the two hybrid classes (γ Dor + δ Scuti vs. δ Scuti + γ Dor) into a single hybrid class regardless of which variability type is more prominent. We also merge the SPB and γ Dor pulsators into a single class, as already motivated in the previous section (additional reasons are discussed below). The remaining classes are the pure δ Scuti pulsators and pure rotational variables (“Rot”). We discard the Skarka sample containing “VAR” sources – stars deemed to be variable with an indeterminate classification.

The majority of the stars in this additional training sample are located in the TESS continuous viewing zone (CVZ), such that each star has multiple sectors of observations up to almost a year in length. On the other hand, our classification sample – the candidate p- and g-mode pulsators – are typically observed in only one or two sectors as a consequence of being distributed randomly across the sky. As a result, we do not stitch the light curves of any of the targets in the training sample. Instead, we compute their features on a per-sector basis and consider each sector of observations as a separate input. That is, a single target in the training sample can contribute to the final sample multiple times. We note that this will lead to larger ambiguity in the classification sample. For example, observations of true γ Dor pulsations might be unresolved in a single sector, such that they are confused with a rotational signal. Likewise, variables such as eclipsing or ellipsoidal variables may have variability periods which exceed the single-sector observations.

4.2. Feature extraction and classification

We apply a uniform processing of each light curve prior to feature extraction. This processing includes applying a Gaussian high-pass filter to remove long-term trends and dividing the light curve by the standard deviation of its flux (Z-scoring) to ensure normality across the light curve sample. Similar to the training sample, each target is classified on a sector-by-sector basis, so that a single target can have multiple classifications across different sectors.

We use a greedy feature-selection algorithm to pick out a sample of 7 highly orthogonal features from the original 22 features calculated. These are the features that best discriminate amongst the variability classes. We also include several additional features we consider important to the classification which are not calculated in PYCATCH22 but are known to help distinguish variability (see, e.g., [Murphy et al. 2019](#)). These features are the skewness of the flux for discriminating eclipsing binaries, as well as the skewness of the amplitude spectrum at frequencies less than 1 d^{-1} , less than 5 d^{-1} , and greater than 5 d^{-1} . The frequency domain skewness indicators measure the effective power contained in different regions of the amplitude spectrum: δ Scuti variables will typically have significantly higher skewness at higher frequencies, and hybrid pulsators will have strong skewness in both regions. Finally, we include the dominant frequency and amplitude of pulsation (in Z-scored units), the Gaia BP-RP colour index, and the Gaia reduced unit weight error.

Figure 5 shows the confusion matrix for our training and test data. For single-sector observations, the classifier appears accurate, especially for hybrid pulsators and rotational variables. Unsurprisingly, the δ Scuti class is strongly confused with the hybrid class since the training sample was mostly based on TESS data exceeding multiple sectors. As a result, not all modes in the hybrid pulsators are resolved in only a single sector. Curiously, the eclipsing binary class has some overlap with the rotational variable class. This is likely because the EB class consists of semi-detached (EA) and W Ursae Majoris (EW) binaries. Only the contact class contains ellipsoidal binaries. Finally, the γ Dor class is weakly confused with the rotational variables. Again, this is expected; a single sector of observations limits the ability to resolve modes, thus the single rotation peak can be mistaken for a γ Dor pulsation and vice-versa.

We run the classifier on our sample of candidate δ Scuti and γ Dor pulsators. Note that we do not classify the β Cep sample which we instead manually inspect. The results of the classifier for the sample along with their class probability are presented in Table 1, with the breakdown of each sample and resulting classification in Table 2. The number of classified stars is slightly less than the number of available light curves discussed in Sec. 2.2 because some light curves are completely dominated by poor data and were discarded from the sample.

It is important to note that a single star observed in multiple sectors will have a classification for each sector in the table. For example, TIC 38458616 has been observed for 13 sectors in the first two years of TESS and has an independent classification per sector. Nine of the sectors predict it to be γ Dor variable, and four predict it to be a contact binary, with the majority of sectors having a low probability for their respective class. A closer inspection of the stitched light curve reveals the target to indeed be a binary system. While stitching individual light curves may give better results for poorly resolved modes, we strive to instead

maintain a uniform input sample for the classifier. We show examples of high probability classifications in Fig. A.1.

Finally, we make an additional cut on the resulting classifications. To ensure that the rotational and eclipsing binary variables are reasonably well-separated from the g-mode pulsators, we apply a data cut such that the second-highest amplitude frequency can not be half of the dominant frequency within a tolerance of 0.01 d^{-1} based on the prewhitening performed in Sec. 3.1. This is done because rotational variables and eclipsing binaries typically show a subharmonic frequency at half the dominant due to their strongly non-sinusoidal light curves. Indeed, for eclipsing binaries, this subharmonic is usually the true frequency. Making this additional cut removes 498 candidates from the γ Dor sample.

Using these classifications, we construct the stacked amplitude spectra. That is, we calculate the amplitude spectrum for each star and stack it according to the dominant pulsation frequency for the classified g-mode sample (γ Dor / SPB), the δ Scuti stars, and the β Cep stars, whose prediction probability is above 0.5. We jointly visualize the γ Dor and SPB sample on the same figure. We show the stacked amplitude spectra in Fig. 6. Each row displays the amplitude spectrum of one star sorted vertically by the dominant pulsation period. For the g-mode sample, we observe two distinct ridges, along with a third very faint ridge. The primary ridge is likely dominated by $\ell = 1$ $m = 1$ g-modes, with the secondary by either lower amplitude $\ell = 2$ modes similar to what was seen by Li et al. (2020) for the *Kepler* data, or caused by the harmonic of the dominant mode. We note that the highest amplitude ridge is likely not all pure dipole modes as the ridge is formed from sorting by the dominant period. Note also the presence of a purely vertical ridge and sidelobes at 1 d^{-1} caused by the known TGLC systematic.

The stacked δ Scuti figure shows four obvious ridges, corresponding to the primary, first and second overtones, and harmonic frequency. These lines are known properties of δ Scuti stars, visualized more commonly in Peterson diagrams (Netzel et al. 2022; Pietrukowicz et al. 2020). Finally, the β Cep sample shows no obvious ridges as expected for these low-order p- and g-mode pulsators (Stankov & Handler 2005).

4.3. Prioritised catalogue of new pulsators ranked by asteroseismic potential

We present a catalogue of all the new pulsators ranked by their asteroseismic potential (Table 3). As an example for the γ Dor variables, we quantify how likely they are to be true γ Dor stars, and how viable we believe their pulsation modes are for typical g-mode analyses (i.e., Li et al. 2020). This table is a combination of the class prediction probability, the number of currently available sectors (calculated using TESS-POINT; Burke et al. 2020), and cuts made based on prewhitening and combination frequency removal. We weigh the contribution to the ‘score’ equally with the following criteria; 1. The number of sectors that the target falls on a TESS camera up to Cycle 6 of TESS observations divided by the maximum number of sectors possible for a CVZ target. 2. The predicted class probability, calculated as the mean probability of each sector. For targets with multiple sectors of observation, we find the mean probability of each predicted class and choose the class with the highest probability. Since the β Cep sample has no predictions, we do not include this in their scoring. 3. the number of observed independent modes found during

the prewhitening process after removal of harmonics and combination frequencies.

We include all columns used to calculate this score for users wishing to prioritize follow-up studies or work with alternative features, and show a few high-probability classifications in Fig. A.1.

Finally, we briefly comment on the overlap of our asteroseismic sample with the sample provided by IJSpeert et al., 2024 (submitted). Their sample consists of 14,573 characterized eclipsing binary systems observed by TESS across the O- to F-type stars. Due to differing selection methods, our overlap consists of only 339 stars. However, a comparison of dominant and secondary frequencies indicates good agreement between the two samples.

5. Conclusions

In this paper we have examined the pulsators of spectral type O, B, A, or F classified from Gaia DR3 photometry by Gaia Collaboration et al. (2023a) and having TESS high-cadence light curves. A comparison of dominant frequencies present in these independent light curves indicates that Gaia is extremely good at measuring g-mode frequencies (approximately 80% precision when compared against TESS), and reasonably effective at higher frequencies (69%). We note that for the higher frequency p-modes, it is unclear whether the Gaia or TESS data is more accurate for measuring the ‘true’ dominant frequency. The 30-minute cadence of the TESS data precludes accurate measurement of signals above 24 d^{-1} , whereas the Gaia photometry suffers from instrumental effects at mmag level and its unequal sampling means there is no clearly defined Nyquist limit. As such, we consider the 69% precision for the p-modes to be a worst-case scenario.

A comparison of amplitudes for the dominant and secondary frequencies for each variable class reveals that γ Dor and SPB variables have indistinguishable amplitude distributions. Prior work on variability classification supports this result. While colour information has been used to distinguish between the two classes of pulsators on the basis of instability computations, Gaia Collaboration et al. (2023a) and Aerts et al. (2023) found there to be a ‘continuum’ of g-mode pulsators bridging the predicted strips. Said differently, both Gaia DR3 and TESS reveal that g-mode pulsators occur along the main sequence covering an effective temperature ranging from roughly 6500 K to 18 000 K. According to instability computations available in the literature, a fraction of these g-mode pulsators are too cold to be SPB stars and too hot to be γ Dor stars. The large ranges in effective temperature and luminosity for the Gaia DR3 γ Dor and SPB stars discussed in Aerts et al. (2023) and now confirmed with TESS point to a lack of physical ingredients in excitation predictions, such as rotation, radiative levitation, nonlinear mode coupling (and tidal mode excitation not discussed here). The combined Gaia DR3 and TESS light curves make us conclude that there is one large global region of g-mode pulsations excited along the main sequence, which is likely caused by a multitude of non-exclusive physical phenomena. This suggestion from Aerts et al. (2023) is now solidified here from our confirmation of the nature of these g-mode pulsators in our catalogue, thanks to their TESS light curves. We also note that although g-modes appear to be found across that entire temperature range, not all stars pulsate in g-modes and not all pulsators are hybrids.

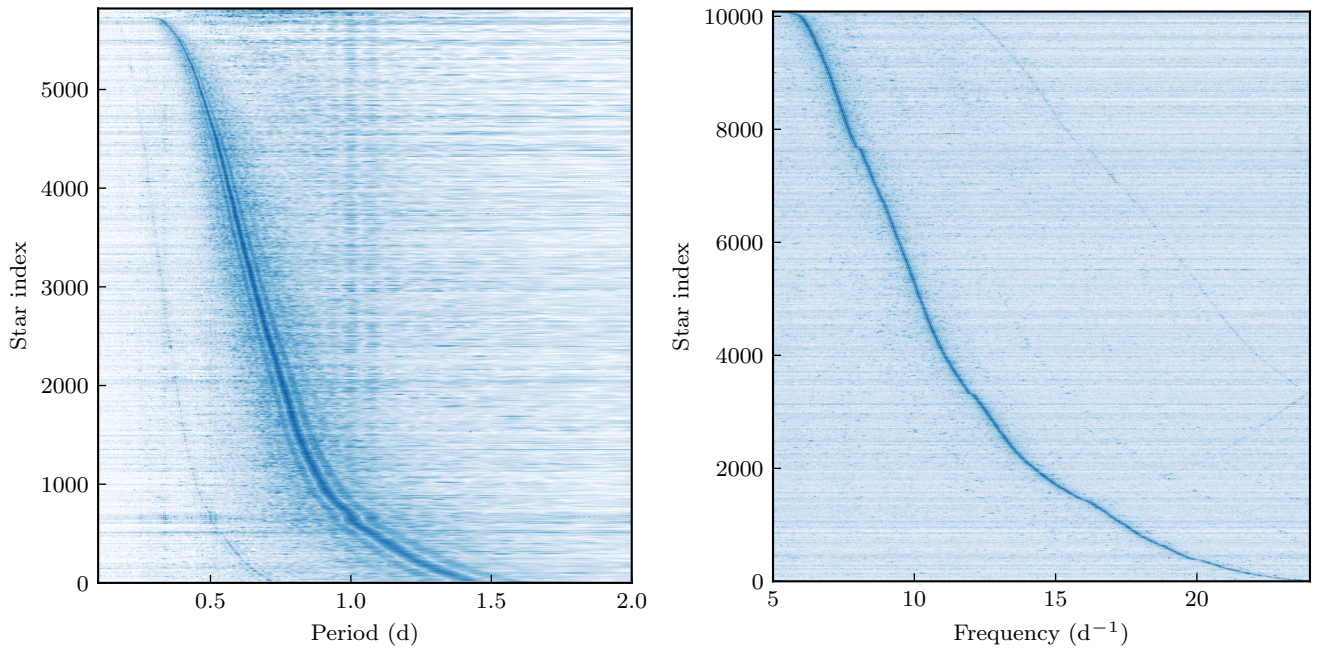


Fig. 6. Stacked amplitude spectra of the g-mode candidate sample (left, in period space) and δ Scuti candidate sample (right, in frequency space) for which the prediction probability is greater than 0.5. Each star forms a single row, sorted by the dominant pulsation, with color corresponding to amplitude. For the g-mode sample, which combines both γ Dor and SPB stars, we see a distinct secondary ridge associated with either a harmonic of the dominant frequency or the expected $\ell = 2$ dipole modes seen in Li et al. (2020). For the δ Scuti sample, we see ridges associated with the first and second overtones, as well as a harmonic line.

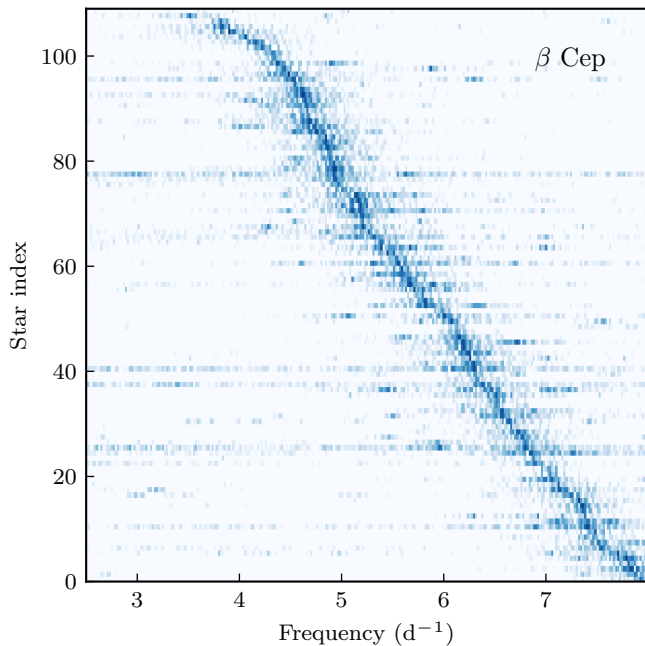


Fig. 7. Stacked amplitude spectra of the β Cep sample sorted by dominant pulsation frequency for those class members whose dominant mode occurs between 3 and 8 d⁻¹.

The classification of the TESS light curves reveals that the original Gaia variability classification done by Coordination Unit 7 of the mission (see Holl et al. 2018; Gaia Collaboration et al. 2019; Eyer et al. 2023; Rimoldini et al. 2023; Gaia Collaboration et al. 2023a) is remarkably accurate. For each candidate

variable from Gaia, we find that the majority of their TESS light curve classifications are in good agreement with their Gaia classification. These results point to around 6,000 new γ Dor, 20,000 new δ Scuti, and 1,481 new SPB pulsators confirmed by TESS. While the TESS light curve classification is expected to be more accurate than Gaia, we note that it is not perfect. Notably, the low-frequency g-mode pulsators are easily confused with rotational variables.

We have made available several tables and datasets from the results of this paper, including; prewhitened frequencies, amplitudes (in Gaia and TESS), phases, and false alarm levels to 1% significance level for every target, classifications and their respective probabilities for each sector of observation, and a rank-ordered table of useful candidate pulsators. It is our hope that the results presented here will enable future ensemble asteroseismic studies of hot non-radial pulsators on the main sequence, especially with the release of Gaia DR4 and DR5, as well as with the upcoming PLATO mission (Rauer et al. 2024).

Acknowledgements. The authors thank Timothy Bedding for helpful comments and discussions. The research leading to these results has received funding from the KU Leuven Research Council (grant C16/18/005: PARADISE) and from the European Research Council (ERC) under the Horizon Europe programme (Synergy Grant agreement N^o 101071505: 4D-STAR). While partially funded by the European Union, views and opinions expressed are however those of the author(s) only and do not necessarily reflect those of the European Union or the European Research Council. Neither the European Union nor the granting authority can be held responsible for them. This research was supported by the Munich Institute for Astro-, Particle and BioPhysics (MIAPbP) which is funded by the Deutsche Forschungsgemeinschaft (DFG, German Research Foundation) under Germany's Excellence Strategy – EXC-2094 – 390783311. The MIAPbP research program facilitated the interactions between the two authors, which ultimately led to the current paper.

Table 3. Rank ordered tables for the γ Dor, δ Scuti, and SPB, and β Cep classified pulsators. Note that the tables are separated according to their candidate and classification status – g-mode pulsators are the g-mode candidates from Aerts et al. (2023), and the p-mode pulsators are the candidates from Gaia Collaboration et al. (2023a). In the table, P and N_f refer to the probability of the classification and the number of independent modes respectively. Sectors is the number of non-contiguous sectors in which the target falls on TESS cameras calculated up to Cycle 6. The full version in electronic format is available online.

<i>γ Dor sample</i>													
TIC ID	DR3 ID	RA	Dec	Prediction	P	N_f	f_1	f_2	A_1	A_2	Sectors	Score	
		deg	deg			d^{-1}	d^{-1}	ppt	ppt				
326258494	2249180128450868992	298.84	67.87	GDOR/SPB	0.98	17	2.62	2.24	12.21	0.72	37	0.79	
259127682	2260889652408354944	291.59	67.19	GDOR/SPB	0.84	24	1.08	1.18	9.07	4.61	36	0.79	
364588332	4648571270586910976	85.13	-75.69	GDOR/SPB	0.91	22	1.31	1.30	9.71	5.38	35	0.79	
<i>δ Scuti sample</i>													
TIC ID	DR3 ID	RA	Dec	Prediction	P	N_f	f_1	f_2	A_1	A_2	Sectors	Score	
233617727	2253706710446026496	284.02	64.80	DSCT	0.75	26	13.02	13.09	15.41	3.60	36	0.77	
176960346	5266903384176544640	101.21	-70.16	DSCT	0.60	37	6.54	10.97	14.79	2.83	33	0.77	
38461275	4670142206953240448	61.21	-64.17	DSCT	0.62	36	9.82	10.53	8.04	2.46	32	0.76	
<i>SPB sample</i>													
TIC ID	DR3 ID	RA	Dec	Prediction	P	N_f	f_1	f_2	A_1	A_2	Sectors	Score	
267543987	2264463198340787968	289.43	72.95	GDOR/SPB	0.62	16	1.28	1.00	20.90	0.57	36	0.66	
349784439	5288831253807922560	113.20	-62.78	GDOR/SPB	0.79	7	2.98	1.49	7.93	5.09	34	0.63	
300382254	5269074232447890048	111.28	-67.76	GDOR/SPB	0.64	14	1.24	0.62	16.69	0.80	34	0.63	
<i>β Cep sample</i>													
TIC ID	DR3 ID	RA	Dec	Prediction	P	N_f	f_1	f_2	A_1	A_2	Sectors	Score	
145594454	5328039318762759552	132.55	-49.00	—	—	40	5.71	5.80	15.24	8.36	6	0.49	
276171115	2055651749653738112	303.31	34.02	—	—	34	5.21	5.12	15.52	4.23	8	0.46	
90964721	2055288395420325760	302.00	33.67	—	—	34	4.06	3.69	12.94	1.54	8	0.46	

References

- Aerts, C. 2021, *Reviews of Modern Physics*, 93, 015001, doi: [10.1103/RevModPhys.93.015001](https://doi.org/10.1103/RevModPhys.93.015001)
- Aerts, C., Christensen-Dalsgaard, J., & Kurtz, D. W. 2010, *Asteroseismology*, Springer-Verlag Heidelberg
- Aerts, C., Cuypers, J., De Cat, P., et al. 2004, *Astronomy and Astrophysics*, 415, 1079, doi: [10.1051/0004-6361:20034628](https://doi.org/10.1051/0004-6361:20034628)
- Aerts, C., Molenberghs, G., & De Ridder, J. 2023, *Astrophysical Properties of 15062 Gaia DR3 Gravity-Mode Pulsators: Pulsation Amplitudes, Rotation, and Spectral Line Broadening*, arXiv, doi: [10.48550/arXiv.2302.07870](https://doi.org/10.48550/arXiv.2302.07870)
- Aerts, C., & Rogers, T. M. 2015, *ApJ*, 806, L33, doi: [10.1088/2041-8205/806/2/L33](https://doi.org/10.1088/2041-8205/806/2/L33)
- Aerts, C., & Tkachenko, A. 2024, *A&A*, in press, arXiv:2311.08453, doi: [10.48550/arXiv.2311.08453](https://doi.org/10.48550/arXiv.2311.08453)
- Aerts, C., Molenberghs, G., Michielsen, M., et al. 2018, *ApJS*, 237, 15, doi: [10.3847/1538-4365/aaccfb](https://doi.org/10.3847/1538-4365/aaccfb)
- Antoci, V., Cunha, M. S., Bowman, D. M., et al. 2019, *MNRAS*, 490, 4040, doi: [10.1093/mnras/stz2787](https://doi.org/10.1093/mnras/stz2787)
- Audenaert, J., Kuzlewicz, J. S., Handberg, R., et al. 2021, *The Astronomical Journal*, 162, 209, doi: [10.3847/1538-3881/ac166a](https://doi.org/10.3847/1538-3881/ac166a)
- Balona, L. A. 2015, *MNRAS*, 447, 2714, doi: [10.1093/mnras/stu2651](https://doi.org/10.1093/mnras/stu2651)
- . 2016, *MNRAS*, 457, 3724, doi: [10.1093/mnras/stw244](https://doi.org/10.1093/mnras/stw244)
- . 2024, *ApJ*, submitted, arXiv:2310.09805, doi: [10.48550/arXiv.2310.09805](https://doi.org/10.48550/arXiv.2310.09805)
- Balona, L. A., & Dziembowski, W. A. 2011, *MNRAS*, 417, 591, doi: [10.1111/j.1365-2966.2011.19301.x](https://doi.org/10.1111/j.1365-2966.2011.19301.x)
- Balona, L. A., Cunha, M. S., Kurtz, D. W., et al. 2011a, *MNRAS*, 410, 517, doi: [10.1111/j.1365-2966.2010.17461.x](https://doi.org/10.1111/j.1365-2966.2010.17461.x)
- Balona, L. A., Pigulski, A., De Cat, P., et al. 2011b, *MNRAS*, 413, 2403, doi: [10.1111/j.1365-2966.2011.18311.x](https://doi.org/10.1111/j.1365-2966.2011.18311.x)
- Balona, L. A., Handler, G., Chowdhury, S., et al. 2019, *MNRAS*, 485, 3457, doi: [10.1093/mnras/stz586](https://doi.org/10.1093/mnras/stz586)
- Barbara, N. H., Bedding, T. R., Fulcher, B. D., Murphy, S. J., & Van Reeth, T. 2022, *Monthly Notices of the Royal Astronomical Society*, 514, 2793, doi: [10.1093/mnras/stac1515](https://doi.org/10.1093/mnras/stac1515)
- Bedding, T. R., Murphy, S. J., Hey, D. R., et al. 2020, *Nature*, 581, 147, doi: [10.1038/s41586-020-2226-8](https://doi.org/10.1038/s41586-020-2226-8)
- Bedding, T. R., Murphy, S. J., Crawford, C., et al. 2023, *ApJ*, 946, L10, doi: [10.3847/2041-8213/acc17a](https://doi.org/10.3847/2041-8213/acc17a)
- Bell, K. J., Hermes, J. J., Vanderbosch, Z., et al. 2017, *The Astrophysical Journal*, 851, 24, doi: [10.3847/1538-4357/aa9702](https://doi.org/10.3847/1538-4357/aa9702)
- Bouabid, M. P., Dupret, M. A., Salmon, S., et al. 2013, *MNRAS*, 429, 2500, doi: [10.1093/mnras/sts517](https://doi.org/10.1093/mnras/sts517)
- Bowman, D. M. 2020, *Frontiers in Astronomy and Space Sciences*, 7, 70, doi: [10.3389/fspas.2020.578584](https://doi.org/10.3389/fspas.2020.578584)
- Bowman, D. M., Burssens, S., Simón-Díaz, S., et al. 2020, *A&A*, 640, A36, doi: [10.1051/0004-6361/202038224](https://doi.org/10.1051/0004-6361/202038224)
- Bowman, D. M., Buysschaert, B., Neiner, C., et al. 2018, *A&A*, 616, A77, doi: [10.1051/0004-6361/20183037](https://doi.org/10.1051/0004-6361/20183037)
- Bowman, D. M., Kurtz, D. W., Breger, M., Murphy, S. J., & Holdsworth, D. L. 2016, *Monthly Notices of the Royal Astronomical Society*, 460, 1970, doi: [10.1093/mnras/stw1153](https://doi.org/10.1093/mnras/stw1153)
- Bowman, D. M., Burssens, S., Pedersen, M. G., et al. 2019, *Nature Astronomy*, 3, 760, doi: [10.1038/s41550-019-0768-1](https://doi.org/10.1038/s41550-019-0768-1)
- Breger, M. 2000, 210, 3
- Briquet, M., Hubrig, S., De Cat, P., et al. 2007, *A&A*, 466, 269, doi: [10.1051/0004-6361:20066940](https://doi.org/10.1051/0004-6361:20066940)
- Brunsdon, E., Pollard, K. R., Wright, D. J., De Cat, P., & Cottrell, P. L. 2018, *Monthly Notices of the Royal Astronomical Society*, 475, 3813, doi: [10.1093/mnras/sty034](https://doi.org/10.1093/mnras/sty034)
- Burke, C. J., Levine, A., Fausnaugh, M., et al. 2020, *TESS-Point: High precision TESS pointing tool*, *Astrophysics Source Code Library*. <http://ascl.net/2003.001>
- Burssens, S., Bowman, D. M., Aerts, C., et al. 2019, *MNRAS*, 489, 1304, doi: [10.1093/mnras/stz2165](https://doi.org/10.1093/mnras/stz2165)
- Burssens, S., Simón-Díaz, S., Bowman, D. M., et al. 2020, *A&A*, 639, A81, doi: [10.1051/0004-6361/202037700](https://doi.org/10.1051/0004-6361/202037700)
- Burssens, S., Bowman, D. M., Michielsen, M., et al. 2023, *Nature Astronomy*, 7, 913, doi: [10.1038/s41550-023-01978-y](https://doi.org/10.1038/s41550-023-01978-y)
- Cantiello, M., & Braithwaite, J. 2019, *ApJ*, 883, 106, doi: [10.3847/1538-4357/ab3924](https://doi.org/10.3847/1538-4357/ab3924)

Appendix A: Example classified light curves

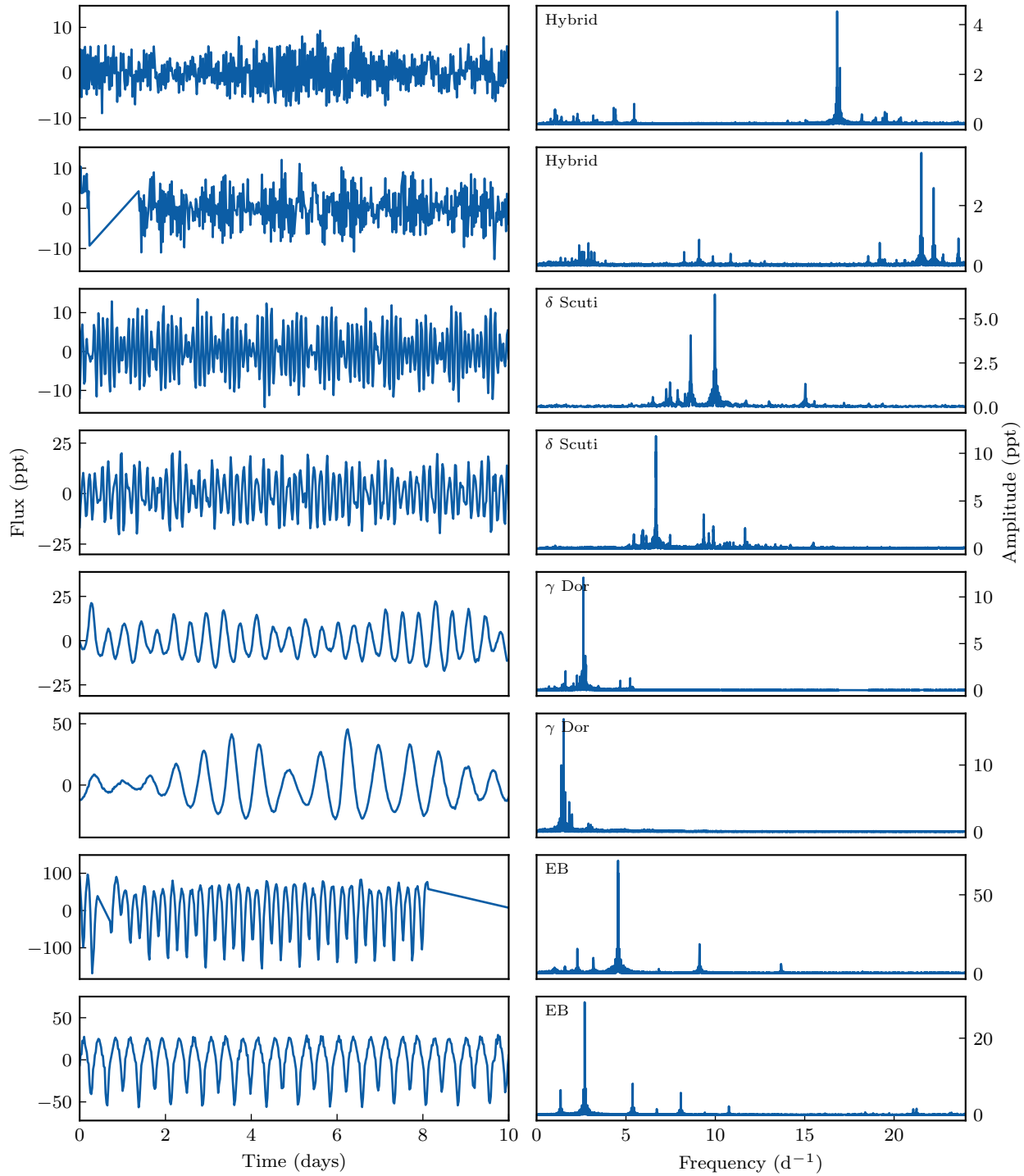


Fig. A.1. A series of prototypical classified light curves from Sec. 4.2, where the classification probability is greater than 0.8. Note that we have stitched multiple TESS sectors to increase the frequency resolution.